# Slow-moving landslides triggered by the 2016 Mw 7.8 Kaikōura earthquake, New Zealand: a new InSAR phase-gradient based time-series approach

Yunmeng Cao[1], Ian Hamling[1], Chris Massey[1], Phaedra Upton[1]

[1]GNS Science, Lower Hutt, New Zealand

**Key Points:**

- A new InSAR phase-gradient based time-series approach used to detect earthquake-triggered slow-moving landslides
- 21 slow-moving landslides triggered by the 2016 Mw 7.8 Kaikōura earthquake are detected and monitored
- Our results reveal decaying characteristics of post-seismic velocity of the earthquake-triggered slow-moving landslides

**Abstract** Earthquake-triggered slow-moving landslides are not well studied mainly due to lack of high-resolution in-situ geodetic observations both in time and space. Satellite-based interferometric synthetic aperture radar (InSAR) has shown potential in landslides applications, however, it is challenging to detect earthquake-triggered slow-moving landslides over large areas due to the effects of post-seismic tectonic deformations, atmospheric delays, and other spatially propagated errors (e.g., decorrelation noises caused unwrapped errors). Here, we present a novel InSAR phase-gradient-based time-series approach to detect slow-moving landslides that triggered by the 2016 Mw 7.8 Kaikōura earthquake. 21 earthquake-triggered large (> 0.1 $km^2$) slow-moving landslides are detected and studied. Our results reveal decaying characteristics of the temporal evolutions of these landslides, that averagely after 3.9 years since the earthquake, their post-seismic velocity will decay 90% and close to pre-seismic level. Our study opens new perspectives for the research of the mass balance of earthquakes and helps reduce associated hazards.

**Plain Language Summary** Large shallow earthquakes in mountainous regions can trigger widespread landslides that cause major damage to infrastructure. Such landslides are typically identified using aerial imagery, optical satellite images, or fieldwork as such landslides tend to be associated with ‘fresh’ scars and deposits of debris. However, there are also another type of landslides, that triggered by earthquake but move slowly, are difficult to find and monitor. Satellite-based interferometric synthetic aperture radar (InSAR) provides an opportunity to monitor slow-moving landslides, however, given the weak and localized signals in the InSAR maps, the landslide displacements are easily contaminated by other signals in InSAR. To address this problem, we developed a new InSAR-phase-gradient based time-series method. Using our

new method, we find 21 large earthquake-triggered slow-moving landslides with average area of 0.84 $km^2$. Through studying the spatio-temporal displacements of these landslides, we find their movements gradually recover to pre-seismic level in the years after the earthquake. Our study helps us to better understand the mechanism of earthquake triggered landslides, and thus help to reduce associated hazards.

## 1. Introduction

Large shallow earthquakes in tectonically active mountain chains can trigger widespread landslides that cause major damage to properties and infrastructure (e.g., Hovius, Stark and Allen 1997, Massey et al. 2018, Bontemps et al. 2020). Although most earthquake-triggered landslides initiate as a result of the inertia forces from the earthquake acting on the slope (Keefer 1984, Jibson et al. 1994, Huang and Li 2014, Fan et al. 2019), others may continue to move slowly (e.g., millimeter to several meters per year) after the shaking from the earthquake attenuates and can continue to move for months to decades (Lacroix et al. 2014). Various mechanisms of landsliding under seismic forcing have been presented: perturbation of the basal friction during and after the shaking (Moro et al. 2011, Lacroix et al. 2014); co-seismic weakening of substrate material (Dadson et al. 2004); increased pore water pressure due to the crushing of the grains in the shearing plane (Jibson et al. 1994, Wasowski et al. 2002). These mechanisms, however, are still not well validated due to lack of high-resolution in-situ geodetic observations both in space and time. While there are a few examples where Global Positioning Systems (GPS) monitoring have been used to track slow-moving landslides following earthquakes (Lacroix et al. 2014, Bontemps et al. 2020), it is not a routine method that can be used to monitor earthquake-triggered landslides.

The movement patterns of rapid (typically >1.8 m/hour, Hungr et al., 2014) co-seismic landslides are difficult to monitor in near real time due to their velocity of movement and disaggregated nature of their debris – as most tend to be debris and rock avalanches and flows (e.g., Keefer, 1984; Massey et al., 2021). The movement patterns of coherent (Keefer, 1984), co-seismic landslides during and after an earthquake are also difficult to monitor using in-situ geodetic techniques as the location of where the landslide might occur needs to be known prior to the earthquake, to allow equipment to be installed. Even if a landslide is pre-existing and monitoring equipment is installed on it, to capture its reactivation during an earthquake, requires an earthquake – with ground shaking large enough to trigger movement – to occur during the lifetime of the monitoring. Remote sensing datasets combined with digital image correlation and deep learning techniques can be used to derive landslide movement patterns from pre- and post-landslide movement, optical image and lidar surveys (e.g., Senogles et al., 2022), however, such techniques lack the temporal resolution to identify the changes in landslide movement patterns over time, therefore not allowing patterns of movement to be linked to their causes. As a result of these constraints: 1) the movement patterns

at high temporal resolutions of coherent landslides, in response to, and after strong ground shaking remain largely unknown; and 2) the mechanisms governing such displacements are poorly understood. Most coherent slides and slumps are typically assumed to displace via 'sliding block' style mechanisms (e.g., Newmark 1965). Such mechanisms assume sliding occurs along a plane, with or without internal deformation of the sliding mass (e.g., Makdisi and Seed, 1978). In such analyses, permanent slope displacement occurs when the acceleration of the slope, caused by the earthquake inertia forces, is larger than the yield acceleration of the slope. Movement of the landslide is assumed to stop when the earthquake accelerations are below the yield acceleration. However, movement of the landslide could continue if for example, the coseismic displacement causes a change in the strength of the moving mass and/or a change in pore-water pressures within the mass. Earthquake-induced landslides, could therefore in theory, continue to move after an earthquake.

Satellite-based interferometric aperture radar (InSAR) techniques are increasingly being used to monitor slow-moving landslides (Schlögel et al. 2015, Sun et al. 2015, Dai et al. 2016, Bekaert et al. 2020), over large areas (e.g., ~ 250 km) with high spatial resolution (e.g., ~ 10 m). However, it is still challenging to use current InSAR techniques to detect earthquake-triggered slow-moving landslides because of at least three reasons: 1) the locations of these landslides are often unknown and their distributions can cover large areas (e.g., up to 100 km away from the epicenter); 2) the weak (e.g., several centimeters per year) and local (e.g., ~ 1 km) landslide deformations would be largely contaminated by atmospheric delays (e.g., Cao, Jónsson and Li 2021, Cao et al. 2017) and post-seismic deformation; and 3) possible unwrapping errors mainly caused by decorrelation noises particularly over dense vegetation regions (e.g., Yunjun, Fattahi and Amelung 2019), usually cause large uncertainties or even wrong values in InSAR-derived time-series results (e.g., velocity map or time-series displacements), especially when the pixel of interest is far away from the reference pixel due to the spatially propagated characteristics of the unwrap errors.

To address the above-mentioned problems for hunting and monitoring earthquake-triggered slow-moving landslides over large areas, here we propose a new InSAR phase-gradient based time-series approach. We use the phase gradient directly calculated from wrapped interferograms, and we estimate time-series solutions of the displacement-gradients by using multi-temporal phase-gradients from those interferograms with short-baselines. We identify earthquake-triggered slow-moving landslides by analyzing the displacement-gradient velocities before and after the earthquake, and we explore temporal evolutions of these landslides using time-series solutions of the displacement-gradients. Advantages of our new method include: 1) effects of those spatial correlated large-scale signals (e.g., atmospheric delays and post-seismic deformations) are minimized; 2) our results are not affected by unwrap errors and the quality of the time-series products (e.g., gradient velocities, or time-series solutions of displacement-gradients) can be well

evaluated; and 3) temporal evolutions of the landslides can be analyzed directly from time-series of the gradient.

Using the new method, we identify and investigate slow-moving landslides triggered by the 14 November 2016 Mw 7.8 Kaikōura earthquake, New Zealand, which is one of the most complex earthquakes ever recorded (e.g., Hamling et al. 2017, Xu et al. 2018). More than 29,000 mapped landslides were triggered by the Kaikōura earthquake over an area of about 10,000 km$^2$. Most were mapped using aerial imagery, optical satellite images, and DEM differences, and most comprised rapid debris and rock avalanches (Massey et al. 2018, Massey et al. 2020). In contrast to these landslides, many large coherent landslides were already present on the slopes, which were strongly shaken by the 2016 Kaikōura earthquake. Most of these landslides can be classified as rock slides or slumps (Hungr et al., 2014), but their activity rates before, during and after the Kaikōura earthquake were largely unknown. Given the 'coherent' morphology of these landslides it could be assumed that they move relatively slowly (Hunger et al., 2014), or rapidly over very short time periods, thus giving the impression that they are either dormant or creeping, and/or move episodically in response to strong earthquake shaking. In this paper we focus on these large coherent rock slides/slumps, which are assumed to be slowly moving and could be either first-time failures (initiated by the 2016 Kaikoura earthquake) or reactivated by the earthquake. Hereafter, for simplicity, we define these earthquake-triggered slow-moving landslides as eSMLs.

## 2. Methods

InSAR phase gradients calculated from wrapped interferograms can be written as:

$$\begin{cases} \Delta\varphi^{r}_{i,j} = U\left\{W\{\varphi_{i,j+1}\} - W\{\varphi_{i,j}\}\right\} \\ \Delta\varphi^{a}_{i,j} = U\left\{W\{\varphi_{i+1,j}\} - W\{\varphi_{i,j}\}\right\} \end{cases} \quad \text{where: } U\{x\} = \begin{cases} x + 2\pi\,, & x < -\pi \\ x\,, & -\pi \le x \le \pi \\ x - 2\pi\,, & x > \pi \end{cases}$$

where $\Delta\varphi^{r}_{i,j}$ and $\Delta\varphi^{a}_{i,j}$ are the phase gradient along range direction (i.e., line-of-sight, LOS) and azimuth direction (i.e., flight direction), respectively, $W\{\varphi_{i,j}\}$ denotes the wrapped phase at location $(i,j)$, $U\{x\}$ is the operator of calculating phase gradient from wrapped phase. Here we propose to use multi-temporal phase gradients to analyze the temporal evolutions of those earthquake-associated local deformations, for hunting and monitoring earthquake-triggered slow-moving landslides.

To detect the slow-moving landslides that triggered by the 2016 Mw 7.8 Kaikōura earthquake, we use 166 Sentinel-1 images acquired from ascending track during October 2014 to September 2021 (see Figure S1). We simulate the topographic phase and the flatten earth phase using the 30m Copernicus DEM (https://spacedata.copernicus.eu/), and we remove the simulated components

from the raw interferogram to get the differential interferogram, and we apply 10 and 2 multi-look numbers to the range and the azimuth direction, separately, which derives a spatial resolution of around 30 m for each pixel. Then, we apply an improved Goldstein filter (Li et al. 2008) to the differential interferogram to mitigate the effects of decorrelation noises, and we calculate the phase gradients from the filtered differential interferogram using the above equation. Thus, the main components in the phase gradient include displacement, atmospheric delay, decorrelation noise, DEM errors, and possible orbital error. It should be noted all of these components are the differences between two adjacent pixels, and so spatially correlated long-wavelength of signals are all removed.

We generate the interferometric network based on the baseline thresholds of 80 days and 120 m, and to make sure all of the interferometric pairs are included in one subset, we bridge the network gap that between January and May 2018 by using all of the pairs covering the period of December 2017 to June 2018 constrained by a spatial baseline of 120 m. We estimate the time-series solutions of phase gradients (October 2014 to September 2021) using a weighted least-squares method (Yunjun et al. 2019), and we calculate the weights as follow:

$$\begin{cases} w_{i,j}^{r} = \left[Var\{\varphi_{i,j+1}\} + Var\{\varphi_{i,j}\}\right]^{-1} \\ w_{i,j}^{a} = \left[Var\{\varphi_{i+1,j}\} + Var\{\varphi_{i,j}\}\right]^{-1} \end{cases}$$

where $w_{i,j}^{r}$ and $w_{i,j}^{a}$ are the value of weights that used for time-series estimation, and $Var\{\cdot\}$ means the operator of calculating variance. Because the uncertainty of the interferometric phase is mainly caused by the decorrelation noises, its variance can be modeled based on the coherence and the multilook numbers (Tough, Blacknell and Quegan 1995), in addition, we assume the decorrelation noises are spatially uncorrelated, thus, variance of the phase gradient can be considered as accumulation of the variances of the two interferometric phases. We evaluate the quality of the time-series solutions based on the estimated temporal coherence (Pepe and Lanari 2006), and we mask all of those pixels where the temporal coherences are smaller than 0.6 in further analysis. To correct the DEM errors in the time-series solutions, we estimate the DEM residuals using all of the post-seismic datasets (November 2016 to September 2021) (Fattahi and Amelung 2013), and then we correct the whole time-series based on the estimated the DEM residuals.

To hunt those earthquake-triggered slow-moving landslides signals, we estimate the differences between the pre- and post-seismic velocities of the displacement gradient. Here we use all of the SAR datasets that before the November 2016 earthquake to estimate the pre-seismic gradient velocity, and we use the data that acquired after the earthquake to January 2018 to estimate the post-seismic velocity. Considering displacement-gradients have different sensitivities along the range and the azimuth directions, we fuse the velocity differences that derived from the range gradient and the azimuth directions as follow:

$$\Delta V_{G_N} = \sqrt{\Delta V_{G_r}{}^2 + \Delta V_{G_a}{}^2}$$

where $\Delta V_{G_N}$ is the normalized displacement gradient that used to describe the difference before and after the earthquake; $\Delta V_{G_r}$ and $\Delta V_{G_a}$ are the velocity differences of the displacement gradients before and after the earthquake along the range and the azimuth directions, respectively. By jointly analyzing $\Delta V_{G_N}$ and geomorphology, we then pick up those slow-moving landslides signals. We finally re-estimate and analyze the spatio-temporal displacements of the detected slow-moving landslides one by one, using the regular SBAS (Small BAseline Subset) technique (Berardino et al. 2002), based on the multi-temporal unwrapped interferograms over the local landslide region. Because we solve the time-series of each landslide within a very local area, we consider the effects of the atmospheric delays, unwrap errors, and the seismic tectonic deformations on the time-series solutions are very limited. The workflow of our methods can be summarized as 7 steps (Figure S2).

## 3. Results and modeling

Pre- and post-seismic velocities of the displacement gradients are calculated based on the time-series solutions of the displacement gradients (Figure S3). The normalized gradient velocities ($\Delta V_{G_N}$), are estimated (Figure 1a) by fusing the range- and the azimuth-gradient velocities. We can see that those strong signals of $\Delta V_{G_N}$ are mainly distributed along the ruptures (red line) or active faults (e.g., Clarence fault and London Hill fault) which are close to the main fault ruptures. However, not all of $\Delta V_{G_N}$ signals are associated with eSMLs, with some being caused by short-wavelength afterslip or postseismic rebound. To show the differences in the displacement-gradients before and after the earthquake and to describe the estimation of $\Delta V_{G_N}$, one time-series solutions of the gradients at a specific pixel (see Figure 1a) are illustrated (Figure 1b), and we can see that both the Range- and the Azimuth-gradients fluctuate around zero before the earthquake but increase rapidly after the earthquake, particularly within the first post-seismic year. In addition, we also can find that the magnitudes of the gradients at the two directions show large differences (e.g., the Range-gradients are much smaller than that of the Azimuth-gradients for this case), which indicates that it is necessary to fuse the gradients calculated from the two directions when detecting the earthquake triggered slow movements. Based on the calculated $\Delta V_{G_N}$, we detected 21 eSMLs that were triggered by the 2016 Mw 7.8 earthquake, within an area of about $80 \times 80 km^2$ (see Area 1 and Area 2 in Figure 1a).

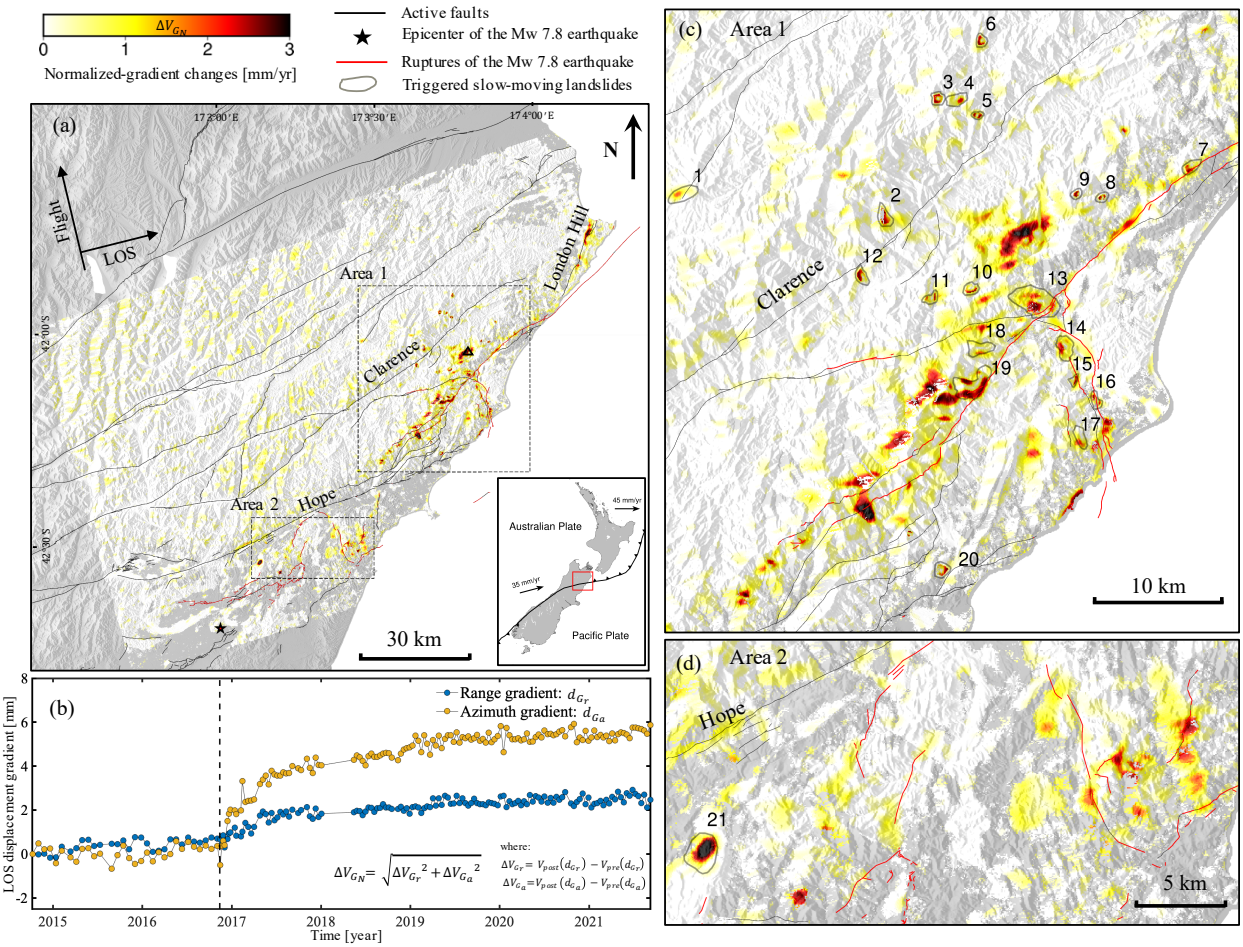


Figure 1. Normalized gradient velocities ($\Delta V_{G_N}$) that indicate the deforming-differences of the gradients before and after the earthquake: (a) detected $\Delta V_{G_N}$ using the ascending Sentinel-1 datasets. The black lines represent the active faults and the red lines represent the ruptures caused by the 2016 earthquake. The right bottom subplot shows the background tectonic setting, and the red rectangular denotes the region of interest; (b) One example (location see black triangle in Figure 1a) of the gradients time-series used to show the calculation of $\Delta V_{G_N}$ and the to present the gradient differences before and after the earthquake. The dashed line means the time of the earthquake; (c) Detected eSMLs over Area 1; (d) Detected eSMLs over Area2.

Time-series evolutions of the gradients and displacements of the detected eSMLs are presented as Figure 2. To pick apart the likely mechanisms driving the displacements, here by assuming the moving direction is approximately along the slope, we have converted the LOS displacements to downslope displacements based on three parameters: SAR incidence angle, slide slope, and the slide aspect angle. The points in each time-series are selected from the central creeping area of the eSMLs with good temporal coherence larger than 0.7. Here we define long-term changes of gradient as positive, and the downslope displacement as negative. We can see that, before the earthquake, both the gradients (Figure 2a and 2b) and the displacements (Figure 2c) of the eSMLs are quite stable and fluctuate around zero (or evolve with a tiny velocity), after that, we can find significant changes in the velocities of the gradients and the displacements, which indicates that the velocity changes in the gradients or the displacements are caused by the 2016 Kaikōura

earthquake. After about 5 years since the earthquake, the accumulated post-seismic range- and azimuth-gradients reach to ~ 8 mm (e.g., the 28$^{th}$ eSML) and ~ 7 mm (e.g., the 4$^{th}$ eSML), respectively, and that of the displacements reach up to 20 cm (e.g., the 10$^{th}$ eSML). It should be noted that the eSMLs with large gradients changes do not mean they have large displacements, as the gradient results represent the differences between the two adjacent pixels within the eSML, whereas that of the displacements represent the integral results of the gradients (e.g., from a stable point outside of the eSML to the pixel of interest inside the eSML).

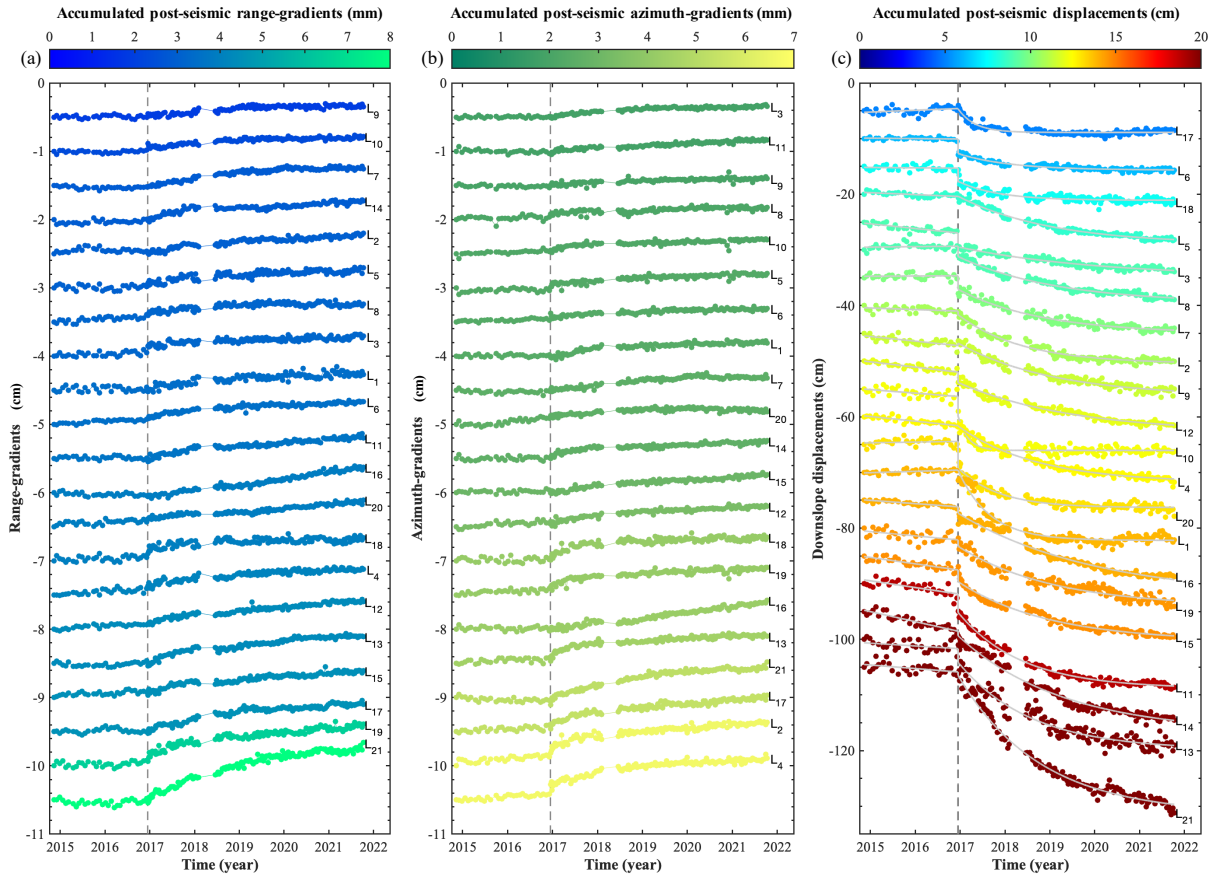


Figure 2. Time-series evolutions of the eSMLs between 2014 and 2021: (a) InSAR derived time-series solutions of the range-gradients; (b) Time-series solutions of the azimuth-gradients; (c) Time-series solutions of the displacements, and the solid gray lines represent the best fitted models. Solid circles denote the estimations at the SAR acquisitions, and the dashed gray lines mean the timing of the earthquake. Curve colors are associated with the maximum accumulated gradients or downslope displacements. The interval of the start gradient of each eSML in (a) and (b) is 2.5 mm, and the interval of the start displacement in (c) is 5 cm.

We also can find that, both the gradients and the displacements showed significant acceleration in the velocities after the earthquake compared with that of pre-seismic, but the velocity gradually recover to pre-seismic levels again after years since the earthquake, this implies that the eSMLs have "self-healing" characteristics. To quantitatively analyze the temporal evolution of the eSMLs, here we propose to use the following piecewise function to model the time-series of downslope displacements

$$\begin{cases} y_{pre}(t) = kt + b \\ y_{post}(t) = \alpha\left(e^{-\beta t} + d_0\right) \end{cases}$$

where $y_{pre}(t)$ is a linear function that denotes the modeled pre-seismic process, and $k$, $b$ are to be estimated parameters; $y_{post}(t)$ is a decay-shaped exponential function that represents the modeled post-seismic process, and $\alpha$, $\beta$, $d_0$ are to be estimated parameters. $\alpha$ and $\beta$ will determine the decay shape, and $d_0$ will determine the shift at the start-point associated with the co-seismic displacement of the eSML and the InSAR observation errors (e.g., decorrelation noise, atmospheric delay). Here we use a least-squares method to estimate those unknown parameters based on the time-series observations. The best fitted models are presented as the solid gray lines in Figure 2c, and the averaging value of the correlations between observations and the models reaches 0.95 (see Table S1), which indicates that the used models are suitable for these eSML cases. Note that the co-seismic displacement is estimated by $y_{co} = y_{post}(t_{EQ}) - y_{pre}(t_{EQ})$, which is challenge to estimate directly from the time-series, due to the effects of observation noises and the timing differences between the SAR acquisition and the earthquake. From the model residuals, we also find seasonal variations in the displacements, and we use a simple annual sine function to model that components and estimate the seasonal amplitude. The averaged pre-seismic velocity of the eSMLs is around 4.4 mm/year (see Table S2), this implies that these eSMLs are quite stable before the earthquake. The averaged co-seismic displacement is 1.40 cm, which is consistent with the previous studies that find few centimeters of co-seismic landslide displacements (Moro et al. 2011, Lacroix et al. 2014). Note that here we can consider those large scale co-seismic displacements, which could be up to tens of meters (Hamling et al. 2017), have been removed from the landslide co-seismic displacement, as we use a local reference point (i.e., non-landslide point) for each eSML to estimate the displacement time-series. The mean seasonal amplitude of the downslope displacement is 1.4 mm, and that of the maximum value even reach up to 7.4 mm (the 13$^{th}$ eSML), which should be mostly caused by the variations in the seasonal rainfalls that cause pore pressure changes on the sliding slope. But we dose not find clear correlations between the mean monthly rainfall (see Table S2) and the seasonal amplitude of the displacement, this indicates that the seasonal variations may be dominated by multiple factors (e.g., geological unit, sliding type).

To quantitatively evaluate the decaying characteristics of the eSMLs, here we calculate the temporal velocity evolutions of each eSMLs based on the first-derivative of the estimated post-sesmic model. Instead of analyzing the full sliding velocity, we calculate and compare the normalized post-seismic velocities only, which can be obtained by

$$v_{post}(t) = e^{-\beta t}$$

where $v_{post}(t)$ is the normalized post-seismic velocities of the eSML, that decays from 1 to 0, and $t$ means the time since the earthquake, $\beta$ is the same parameter as that in the displacement model, which controls the decay speed of the eSML. Post-seismic models of the normalized velocities (Figure 3a) clearly show that the landslide velocities decay rapidly spanning years since the earthquake, and different eSMLs show different decaying speeds, e.g., landslide velocities of the 10th eSML decay to around zero within 1 year since the earthquake, whereas that of the 3rd eSML experiences more than 8 years. The decay-timings (Figure 3b) of the post-seismic velocities reveal that after 6 years since the earthquake, the landslide velocities of the eSMLs all decay at least 85%, and within less than 10 years after the earthquake, all of the eSMLs would decay 95%. Averagely, post-seismic velocity of the eSML decay 90% within around 3.9 years since the earthquake. Spatial distribution of the post-seismic rainfalls over the regions of the eSMLs (gray histograms in Figure 3b) indicate that, the relationship between the rainfalls and the decay-timings is limited.

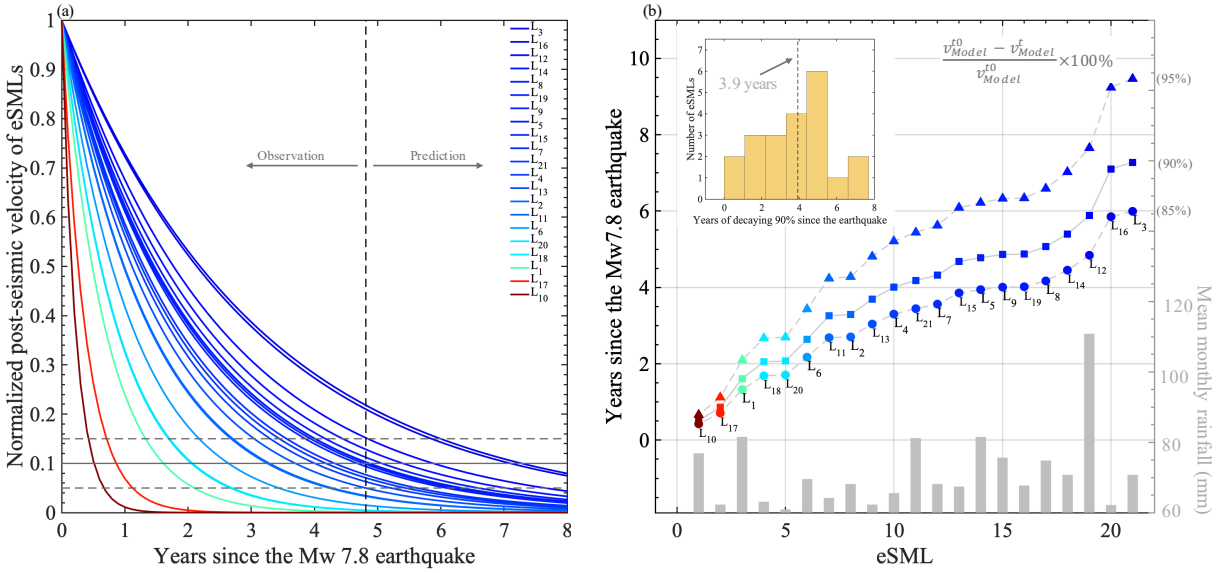


Figure 3 (a) Normalized post-seismic velocity of the eSMLs. The gray lines indicate where the velocities have decayed to 0.15 (decay 85%), 0.1 (decay 90%), and 0.05 (decay 95%), of their maximum. The dashed black line denotes the date of the last SAR observations used in this study. (b) Amount of time for each of the eSMLs to decay to 85% (circle), 90% (rectangular), and 95% (triangle). The gray bars show the average monthly rainfall at the location of each eSML. The histogram in the upper left shows the distribution of decay (90%) times across all of the sSMLs.

## 4. Discussion and Conclusions

We developed a new InSAR-phase-gradient based time-series approach to detect earthquake-triggered slow-moving landslides over large areas, that are difficult to hunt using regular InSAR techniques (e.g., D-InSAR, Stacking-, or SBAS-InSAR) due to the effects of post-seismic tectonic deformations, atmospheric delays, possible unwrapped errors, particularly over vegetated areas. Compared with the previous gradient-stacking methods (e.g., Hu et al. 2020, Fu et al. 2021), the advantages of our new approach include 1) quality of the gradient results can be well evaluated based on the gradient-phase closure of the interferometric network (Samiei-Esfahany et al. 2016), and 2) the DEM errors in the time-series of the displacement-gradients can be corrected. In addition, compared with the velocity-map based gradient method (Bekaert et al. 2020), our method calculates the velocity directly using the phase gradient from the wrapped interferograms, thus our results would not be affected by any unwrapping errors.

Using our new approach, 21 slow-moving landslides triggered by the 2016 Mw 7.8 Kaikōura earthquake were detected, adding to the catalogue of co-seismic landslide failures previously identified (e.g., Massey et al. 2018, Massey et al. 2020). Our results reveal decaying characteristics of the temporal evolutions of these landslides, that averagely after 3.9 years since the earthquake, their post-seismic velocity will decay 90% and recover to a level of near pre-seismic, and this may indicate self-healing of the earthquake-triggered slow-moving landslides in some degree. We suggest that this decay was likely related to a combination of internal deformation of the landslides, as well as slip along their basal slide surfaces, in response to the earthquake-triggered displacement, as post-earthquake landslide displacements did not correlate to rainfall or any other monitored factor.

Adopting the scheme of Hungr, Leroueil and Picarelli (2013), we found most of the landslides (eSMLs) comprise compound planar or rotational slides in rock (see Table S3), which given their size (source area), suggests that their basal slide surfaces could be relatively deep-seated (Massey et al. 2020). Most are relict and reactivated in response to the Kaikōura Earthquake and thus their basal slide surfaces are likely to be either fully formed or at least in part formed. Time-series evolutions of the displacements (Figure 2) show that each eSML is likely to be a function of the local site 'susceptibility' conditions, mainly geological (structure and geomechnical properties) and morphological (slope angle and local slope relief), along with the amplitude and duration of shaking each site experienced during the earthquake (e.g., Massey et al. 2016, Brain et al. 2021). Given the landslide types (reactivations), their sizes (depths), and eSML time-series displacements, we hypothesis that the co-seismic changes in the velocities of the gradients and the displacements are likely to relate mainly to basal sliding mechanisms along with some distributed shear within the overlying slide mass (e.g., Makdisi and Seed 1978, Bray and Travasarou 2007). We also suggest that the post-earthquake time series displacements, given their patterns of displacement,

are more likely to relate mainly to distributed shear within the slide mass material. This is because the exponential decay in displacement, post-earthquake, appears unrelated to seasonal changes in stress caused by rainfall-induced fluctuations in pore-water pressures or subsequent earthquake loading, or any other environmental factor that could initiation movement (Massey, Petley and McSaveney 2013). Such post-seismic deformation might relate to the consolidation of the slide mass, which will be further studied in the future.

Only one ascending track of Sentinel-1 datasets were used in this study, as that of the descending track is not well covered with enough datasets, thus some of the eSMLs signals may not be detected, due to the geometry limitations of InSAR (e.g., shortening and shading) and the 1-D displacement imaging limitation (e.g., InSAR cannot detect those landslides whose sliding direction is vertical to the LOS direction ). In addition, due to the dense vegetation coverage over the Kaikōura region which could cause strong decorrelation noises in InSAR observations, it is challenging to detect small eSMLs (e.g., less than $100m \times 100m$), thus study of these small eSMLs may need to use other SAR datasets which have longer wavelengths (e.g., L-band) and/or higher special resolutions than Sentinel-1. In addition, gradient-based signals are not only associated with eSMLs, but also can be caused by the residual atmospheric delays (i.e., short wavelengths of the atmospheric delays) and some sharp post-seismic deformations, particularly near the earthquake ruptures. The residual atmospheric signals in the gradients can be mitigated by averaging the time-series solutions, but those residual local post-seismic signals are still mixed with the eSMLs in the gradient-velocity maps. To separate the eSMLs from other non-landslide signals in the gradient-results, we subjectively set a threshold value of the normalized-gradient-velocity to determine the potential eSML-regions, thus, we may lose some weak eSML signals in this step, and the number of the detected eSMLs could be underestimated. Deep learning may help to overcome this limitation, which could be considered in our future research.

**Data Availability Statement**

The Sentinel-1 images are from the European Space Agency (ESA) and downloaded from the Alaska Sat- ellite Facility (ASF) (https://asf.alaska.edu/data-sets/sar-data-sets/sentinel-1/). The active fault and ruptures of the 2016 Mw 7.8 Kaikōura earthquake were provided by GNS Science (https://data.gns.cri.nz/af/).The rainfall data was provided by United States Agency for International Development (USAID) (https://data.chc.ucsb.edu/products/CHIRPS-2.0/).

**Reference**


Bekaert, D. P. S., A. L. Handwerger, P. Agram & D. B. Kirschbaum (2020) InSAR-based detection method for mapping and monitoring slow-moving landslides in remote regions with steep and mountainous terrain: An application to Nepal. *Remote Sensing of Environment,* 249.

Berardino, P., G. Fornaro, R. Lanari & E. Sansosti (2002) A new algorithm for surface deformation monitoring based on small baseline differential SAR interferograms. *IEEE Transactions on Geoscience and Remote Sensing,* 40**,** 2375-2383.

Bontemps, N., P. Lacroix, E. Larose, J. Jara & E. Taipe (2020) Rain and small earthquakes maintain a slow-moving landslide in a persistent critical state. *Nat Commun,* 11**,** 780.

Brain, M. J., S. Moya, M. E. Kincey, N. Tunstall, D. N. Petley & S. A. Sepúlveda (2021) Controls on Post-Seismic Landslide Behavior in Brittle Rocks. *Journal of Geophysical Research: Earth Surface,* 126.

Bray, J. D. & T. Travasarou (2007) Simplified procedure for estimating earthquake-induced deviatoric slope displacements. *Journal of geotechnical and geoenvironmental engineering,* 133**,** 381-392.

Cao, Y., S. n. Jónsson & Z. Li (2021) Advanced InSAR Tropospheric Corrections From Global Atmospheric Models that Incorporate Spatial Stochastic Properties of the Troposphere. *Journal of Geophysical Research: Solid Earth,* 126.

Cao, Y., Z. Li, J. Wei, J. Hu, M. Duan & G. Feng (2017) Stochastic modeling for time series InSAR: with emphasis on atmospheric effects. *Journal of Geodesy,* 92**,** 185-204.

Dadson, S. J., N. Hovius, H. Chen, W. B. Dade, J.-C. Lin, M.-L. Hsu, C.-W. Lin, M.-J. Horng, T.-C. Chen, J. Milliman & C. P. Stark (2004) Earthquake-triggered increase in sediment delivery from an active mountain belt. *Geology,* 32.

Dai, K., Z. Li, R. Tomás, G. Liu, B. Yu, X. Wang, H. Cheng, J. Chen & J. Stockamp (2016) Monitoring activity at the Daguangbao mega-landslide (China) using Sentinel-1 TOPS time series interferometry. *Remote Sensing of Environment,* 186**,** 501-513.

Fan, X., G. Scaringi, O. Korup, A. J. West, C. J. Westen, H. Tanyas, N. Hovius, T. C. Hales, R. W. Jibson, K. E. Allstadt, L. Zhang, S. G. Evans, C. Xu, G. Li, X. Pei, Q. Xu & R. Huang (2019) Earthquake-Induced Chains of Geologic Hazards: Patterns, Mechanisms, and Impacts. *Reviews of Geophysics,* 57**,** 421-503.

Fattahi, H. & F. Amelung (2013) DEM Error Correction in InSAR Time Series. *Geoscience and Remote Sensing, IEEE Transactions on,* 51**,** 4249-4259.

Fu, L., Q. Zhang, T. Wang, W. Li & Q. Xu (2021) Detecting active landslides in a large area using InSAR phase-gradient stacking and deep-learning network. *preprint*.

Hamling, I. J., S. Hreinsdottir, K. Clark, J. Elliott, C. Liang, E. Fielding, N. Litchfield, P. Villamor, L. Wallace, T. J. Wright, E. D'Anastasio, S. Bannister, D. Burbidge, P. Denys, P. Gentle, J. Howarth, C. Mueller, N. Palmer, C. Pearson, W. Power, P. Barnes, D. J. Barrell, R. Van Dissen, R. Langridge, T. Little, A. Nicol, J. Pettinga, J. Rowland & M. Stirling (2017) Complex multifault rupture during the 2016 Mw 7.8 Kaikoura earthquake, New Zealand. *Science,* 356.

Hovius, N., C. P. Stark & P. A. Allen (1997) Sediment flux from a mountain belt derived by landslide mapping. *Geology,* 25**,** 231-234.

Hu, X., R. Burgmann, W. H. Schulz & E. J. Fielding (2020) Four-dimensional surface motions of the Slumgullion landslide and quantification of hydrometeorological forcing. *Nat Commun,* 11**,** 2792.

Huang, R. & W. Li (2014) Post-earthquake landsliding and long-term impacts in the Wenchuan earthquake area, China. *Engineering Geology,* 182**,** 111-120.

Hungr, O., S. Leroueil & L. Picarelli (2013) The Varnes classification of landslide types, an update. *Landslides,* 11**,** 167-194.

Jibson, R. W., C. S. Prentice, B. A. Borissoff, E. A. Rogozhin & C. J. Langer (1994) Some observations of landslides triggered by the 29 April 1991 Racha earthquake, Republic of Georgia. *Bulletin of the seismological Society of America,* 84**,** 963-973.

Keefer, D. K. (1984) Landslides caused by earthquakes. *Geological Society of America Bulletin,* 95**,** 406-421.

Lacroix, P., H. Perfettini, E. Taipe & B. Guillier (2014) Coseismic and postseismic motion of a landslide: Observations, modeling, and analogy with tectonic faults. *Geophysical Research Letters,* 41**,** 6676-6680.

Li, Z. W., X. L. Ding, C. Huang, J. J. Zhu & Y. L. Chen (2008) Improved filtering parameter determination for the Goldstein radar interferogram filter. *ISPRS Journal of Photogrammetry and Remote Sensing,* 63**,** 621-634.

Makdisi, F. I. & H. B. Seed (1978) Simplified procedure for estimating dam and embankment earthquake-induced deformations. *Journal of the Geotechnical Engineering Division,* 104**,** 849-867.

Massey, C., F. Della Pasqua, C. Holden, A. Kaiser, L. Richards, J. Wartman, M. J. McSaveney, G. Archibald, M. Yetton & L. Janku (2016) Rock slope response to strong earthquake shaking. *Landslides,* 14**,** 249-268.

Massey, C., D. Townsend, E. Rathje, K. E. Allstadt, B. Lukovic, Y. Kaneko, B. Bradley, J. Wartman, R. W. Jibson, D. N. Petley, N. Horspool, I. Hamling, J. Carey, S. Cox, J. Davidson, S. Dellow, J. W. Godt, C. Holden, K. Jones, A. Kaiser, M. Little, B. Lyndsell, S. McColl, R. Morgenstern, F. K. Rengers, D. Rhoades, B. Rosser, D. Strong, C. Singeisen & M. Villeneuve (2018) Landslides Triggered by the 14 November 2016 Mw 7.8 Kaikōura Earthquake, New Zealand. *Bulletin of the Seismological Society of America,* 108**,** 1630-1648.

Massey, C. I., D. N. Petley & M. J. McSaveney (2013) Patterns of movement in reactivated landslides. *Engineering Geology,* 159**,** 1-19.

Massey, C. I., D. Townsend, K. Jones, B. Lukovic, D. Rhoades, R. Morgenstern, B. Rosser, W. Ries, J. Howarth, I. Hamling, D. Petley, M. Clark, J. Wartman, N. Litchfield & M. Olsen (2020) Volume Characteristics of Landslides Triggered by the Mw 7.8 2016 Kaikōura Earthquake, New Zealand, Derived From Digital Surface Difference Modeling. *Journal of Geophysical Research: Earth Surface,* 125.

Moro, M., M. Chini, M. Saroli, S. Atzori, S. Stramondo & S. Salvi (2011) Analysis of large, seismically induced, gravitational deformations imaged by high-resolution COSMO-SkyMed synthetic aperture radar. *Geology,* 39**,** 527-530.

Newmark, N. M. (1965) Effects of earthquakes on dams and embankments. *Geotechnique,* 15**,** 139-160.

Pepe, A. & R. Lanari (2006) On the Extension of the Minimum Cost Flow Algorithm for Phase Unwrapping of Multitemporal Differential SAR Interferograms. *IEEE Transactions on Geoscience and Remote Sensing,* 44**,** 2374-2383.

Samiei-Esfahany, S., J. E. Martins, F. van Leijen & R. F. Hanssen (2016) Phase Estimation for Distributed Scatterers in InSAR Stacks Using Integer Least Squares Estimation. *IEEE Transactions on Geoscience and Remote Sensing,* 54**,** 5671-5687.

Schlögel, R., C. Doubre, J.-P. Malet & F. Masson (2015) Landslide deformation monitoring with ALOS/PALSAR imagery: A D-InSAR geomorphological interpretation method. *Geomorphology,* 231**,** 314-330.

Sun, Q., L. Zhang, X. L. Ding, J. Hu, Z. W. Li & J. J. Zhu (2015) Slope deformation prior to Zhouqu, China landslide from InSAR time series analysis. *Remote Sensing of Environment,* 156**,** 45-57.

Tough, J. A., D. Blacknell & S. Quegan (1995) A statistical description of polarimetric and interferometric synthetic aperture radar data. *Proceedings of the Royal Society of London,* 449**,** 567-589.

Wasowski, J., V. Pierri, P. Pierri & D. Capolongo (2002) Factors Controlling Seismic Susceptibility of the Sele Valley Slopes: The Case of the 1980 Irpinia Earthquake Re-Examined. *Surveys in Geophysics,* 23**,** 563-593.

Xu, W., G. Feng, L. Meng, A. Zhang, J. P. Ampuero, R. Bürgmann & L. Fang (2018) Transpressional Rupture Cascade of the 2016 Mw 7.8 Kaikoura Earthquake, New Zealand. *Journal of Geophysical Research: Solid Earth,* 123**,** 2396-2409.

Yunjun, Z., H. Fattahi & F. Amelung (2019) Small baseline InSAR time series analysis: Unwrapping error correction and noise reduction. *Computers & Geosciences,* 133.